Contents lists available at ScienceDirect

Chemical Engineering Journal

journal homepage: www.elsevier.com/locate/cej

Flash Joule heating induced highly defective graphene towards ultrahigh lithium ion storage

Shu Dong, Yali Song, Mingyu Su, Guiling Wang, Yingyi Gao, Kai Zhu *, Dianxue Cao *

College of Material Science and Chemical Engineering, Harbin Engineering University, Harbin 150001, China

ARTICLE INFO

Keywords:
Defective graphene
Flash Joule heating
Lithium-ion battery
Capacity rise

ABSTRACT

Introducing defects is an effective approach to promote the lithium ion storage ability of host material. Constructing pure defects is beneficial to understand the lithium ion storage mechanism in the defects. Herein, we fabricate defective graphene without intricate functional groups *via* a flash Joule heating (FJH) technique within a mere 1 ms. The FJH-reduced graphene lattice harbors a multitude of defects, and its unique three-dimensional structural network enables an ultra-high lithium ion storage capacity. Moreover, the highest capacity of F-RGO-5 reaches 2500 mAh/g in the 800th cycle, its three-dimensional architecture allows it to withstand high currents and prolonged cycles without drastic failures. Nascent defects and defect-induced lithium plating predominantly contribute to capacity enhancement during cycling, while dendrite formation primarily leads to decay. Our findings present an approach to defect-based designs of high-capacity lithium anodes and provide valuable insights into their energy storage mechanisms.

1. Introduction

Graphene, a two-dimensional monolayer structure of graphite, is highly anticipated in the energy storage field for its unique electrical properties and nano-size effect [1]. As potential anode materials, especially reduced graphene oxide and heteroatom doped graphene present a capable lithium ion storage behavior. Thus, the lithium ion storage model of graphene is built to support the electrochemical performance beyond expectations. Initially, it was expected that lithium ions would be stored as the LiC_6Li on both sides of single-layer graphene, which leads to a theoretical capacity of 744 mAh/g [2]. However, numerous experiments and simulations have demonstrated that the electrostatic repulsion between lithium ions is significantly stronger than the bonding force between lithium ions and carbon atoms in graphene, making this stoichiometric compound impossible to form [3,4]. Ji's group [5] proved that lithium ions only stored in the interlayer of two graphene layers with the final phase of LiC_{12}, corresponding to a theoretical capacity of 186 mAh/g. This finding breaks the conjecture about graphene's high capacity. Recently, the defect chemistry reveals that the atypical lithium storage behavior and high capacities are attributed to the defects in graphenes [6-8]. Density functional theoretical (DFT) studies suggest that the electron cloud around the carbon atoms near defect sites can accommodate additional electrons, improving the quantum capacitance, and showing a macroscopic increase in capacity [9-11]. Therefore, introducing defects in graphene is a viable strategy to enhance lithium adsorption. However, it is still a challenge to figure out the lithium ion storage mechanism in defective graphene.

The defects in graphene can be divided into intrinsic defects and external defects. The intrinsic defects are caused by the absence or rotation of carbon bonds of six-membered rings and the external defects are produced by heteroatom dopants. The introduced defects could serve as extra lithium ion storage sites, leading to an improved capacity. Usually, the chemical method is carried out to introduce the defects due to the highest defect yield. Graphene oxide (GO) is one of the best precursors for defect engineering and doping engineering, which promise a large number of oxides-induced and adjustable defects [12]. However, it is difficult to remove all the oxygen functional groups on the surface to construct an ideal defective graphene model. The residue would hinder lithium ion and electron transport. In addition, the lithium ion storage behavior is also affected by the heteroatom existence.

Hepported by the Student rein, graphene with multiple vacancy defects is produced *via* the flash Joule heating (FJH) technique. During the FJH process, a large amount of Joule heat generated around the conductive path remove the oxygen-containing functional groups on a microsecond time scale. At the same time, accompanied by the loss of carbon atoms, a large number of defects are produced on the surface of

---

* Corresponding authors.
E-mail addresses: kzhu@hrbeu.edu.cn (K. Zhu), caodianxue@hrbeu.edu.cn (D. Cao).

https://doi.org/10.1016/j.cej.2023.147988
Received 7 August 2023; Received in revised form 20 November 2023; Accepted 8 December 2023

rGO. Most of these defects exhibit considerable formation energy and should not appear in thermal equilibrium, while they can be retained in the FJH process owing to the ultrafast annealing rate. Meanwhile, the F-rGO presents an "insertion-deposition" mixed lithium ion storage mechanism, which leads to a reversible capacity of 2450 mAh/g after 1000 charge–discharge cycles at 1 A/g. The defects in the carbon network, and the local "lithium anode" produced on the surface during the cycle, as well as the partially enclosed three-dimensional structure, synergistically endow the ultra-high capacity and excellent rate performance. Furthermore, by analyzing the capacity changes in different voltage intervals during 5000 cycles, the reason for excess lithium storage in lithium-ion batteries and its fading mechanism was presented. This work provides novel insights into understanding the lithium storage mechanism of defective graphene.

2. Results and discussion

The parameters of the self-assembled FJH equipment are shown in **Figure S1** and **Table S1**. In a typical FJH process, the GO collected by Hummer's method is placed in a quartz tube with openings at both ends. The occurrence of the FJH process is represented by a bright flash emitted from the quartz tube after the energy is released by capacitor banks, and the excess energy is dissipated as blackbody radiation [13,14]. Real-time images of the process are shown in **Figure S2 and Video S1**. The F-rGO displays the interconnected three-dimensional porous features instead of an aggregated cluster of pristine GO, due to a large amount of generated gas escaping from the GO interlayer and shocking away the stacked layers. The discharge parameter is denoted by m@200 V×n, where m represents the number of capacitors that are charged to 200 V and discharged to GO, repeat n times. Four variations of rGO were synthesized employing distinct parameters. These were designated as F-RGO-1, F-RGO-3, F-RGO-5, and F-RGO-1–8, obtained through the FJH processes labeled as 1@200×1, 3@200×1, 5@200×1, and 1@200×8, respectively. Notably, among these, F-RGO-5 exhibit the most separated lamellae, as depicted in Fig. S2**f**. When a higher voltage is applied, thermal shock can break the quartz tube. Additionally, the prolonged flash time induced the re-stacking of rGO, whereby the initially disordered lamellas stacked into dense, short-range organized layers in a specific direction after several small-energy strikes (Fig. S2**g, h**).

The transmission electron microscope (TEM) images (Fig. 1a) show the F-rGO-5 in a folded gauzy shape. Energy-dispersive X-ray spectroscopy (EDS) mapping confirms the removal of oxygen elements from the F-rGO surface, indicating the effective reduction of GO *via* the FJH method (**Figure S3, S4**). The magnified edges of F-rGO-5 exhibit a clear few-layer structure, with some edges presenting as curled, interconnected carbon nanostructures. Moreover, multiple holes appear on the surface, indicating an undulating and rough surface, typically caused by lamellar surface defects (Fig. 1b, c) [15-18]. The adsorption–desorption isotherms for both GO and F-rGO-5 exhibit characteristics aligned with type IV isotherms. The emergence of the H3-type hysteresis loop is ascribed to the layered stacking structure inherent in carbon sheets. As per the Brunauer-Emmett-Teller (BET) method, the specific surface areas of GO and F-rGO-5 measure 3.23 m^2/g^1 and 364.14 m^2/g^1, respectively. This notable increase in specific surface area is attributed to the development of an interconnected three–dimensional

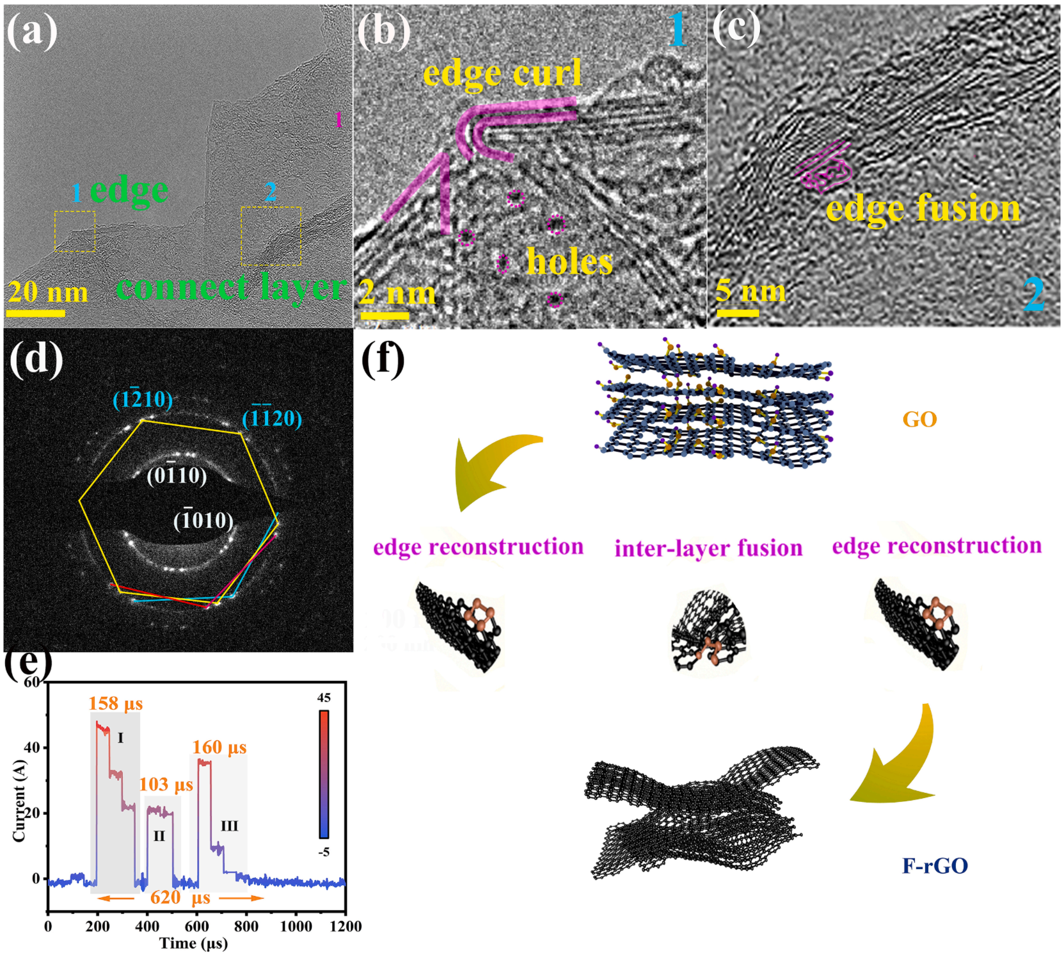

Fig. 1. (a-c) TEM, regional magnification, and (d) SAED pattern of F-rGO-5. (e) Current signal during 5@200 V*1 process. (f) Schematic illustration for the FJH process.

structure. Utilizing the Barret-Joyner-Halenda (BJH) model, the pore size distribution analysis of F-rGO-5 predominantly falls within the range of 2–5 nm, indicating a highly abundant porous framework. Corresponding selected-area electron diffraction (SAED) spots with high brightness display a classical hexagonal distribution, signifying a hexagonal crystalline structure (Fig. 1d). The multiple concentric rings observed in SEAD are the result of stacking or folding of carbon layers [19]. Notably, there are several sets of sixfold symmetrical bright spots in the circle, which rotate relative to each other. These bright spots represent atypical Bernal (AB) stacking of the F-rGO layers, resulting from small angular rotations between multiple planes or the bending of graphene edges, as illustrated in the TEM result [18,20]. The undulating surface in the AFM image also demonstrates the unevenness of the graphene surface (**Figure S6**).

Through the use of a Hall device in conjunction with an oscilloscope and a signal acquisition interval of 0.1 μs, we were able to capture the current signal during the 5@200 V×1 process. The I-t curve (Fig. 1e) demonstrated that the FJH process was complete in a remarkably short time, taking only 620 μs, which is much faster than other commonly used reduction methods. The step-like current signal reveals a three-stage reaction, as depicted in Fig. 1f. During the initial stage, the current step undergoes a sharp spike at 45 A, followed by a rapid decline to 0 A in just 158 μs. After the capacitive switch is turned on, a large number of electrons are released and governed by Fowler-Nordheim tunneling under a high bias [21]. Initially, the electrons preferentially travel along the basal plane, which offers the lowest resistance, thereby generating a significant amount of Joule heat along the conductive pathway. This process sequentially removes adsorbed water, epoxide (C–O–C), hydroxyl, and carboxyl groups (C–OH, COOH) from the GO layers [22,23]. The resulting expanding gas serves to separate the GO layers and, in turn, obstructs the current flow. Thus, the current during the first stage manifests as three distinct steps. Subsequently, as the GO layers come into contact again under the pressure of the spring, the electrons continue to travel along the conductive path, resulting in a secondary FJH process, which represents the second stage. Finally, the oxygen-containing functional groups between the interlayers decrease substantially, and the distance between the lamellae starts decreasing. The dangling bonds at the edges and interlayers are easily built together during Joule heating, resulting in the generation of a current response along the conducting network. Under the guidance of the current, fusion occurs at the interface overlap, and reconstruction occurs at the edge, leading to the formation of a 3D RGO network [24]. In general, the conductivity of multilayer graphene is higher along the direction parallel to the layers as compared to the perpendicular direction. However, in the case of F-rGO structures, the electron pathway is augmented, thereby enhancing the overall conductivity of graphene. The resistance of the reactor also shows a significant decrease before and after the FJH process (**Figure S7**) (22.9 kΩ decreased to 0.6 Ω).

To gain a better understanding of the structural characteristics of F-rGO, further tests were conducted. The XRD pattern of GO (Fig. 2a) shows a sharp peak at 12°, which according to the Bragg equation corresponds to 7.37 Å, much larger than that of graphite (3.37 Å) [25]. This indicates that the original graphite is successfully exfoliated and intercalated. After the FJH process, the characteristic peak of obtained rGO shift to a larger diffraction angle (26.2–26.4°), indicating the removal of the intercalated functional groups, and a significant broadening of the peak due to distortion in the RGO lattice. The RGO layer spacing increases with the one-time released energy. Sharp diffraction peaks at 11.5° and 26.1° appear after eight strikes, representing the re-emergence of AB stacking of rGO from disordered structures to graphite-like structures during multiple FJH strikes, which is also consistent with the changes in morphology observed by SEM (Fig. S2**h**). Compared to GO, the oxygen-containing functional groups in F-rGO-5 are significantly reduced. This is evidenced by the disappearance of broad peaks at 3390 cm^{-1} (–OH, from carboxyl and hydroxyl groups grafted on GO and absorbed water molecules) and sharp peaks at 1249 and 1151 cm^{-1} (ν C–O–C) in the Fourier-transform infrared spectroscopy (FT-IR) spectrum (Fig. 2b) after the reaction. Some incompletely reacted oxygen-containing functional groups make the peak (1677 cm^{-1} (ν C=O)) not completely disappear, which cannot be avoided by using GO as a precursor [26,27]. The ultra-high carbon content in F-rGO-5 is further confirmed by high-resolution X-ray

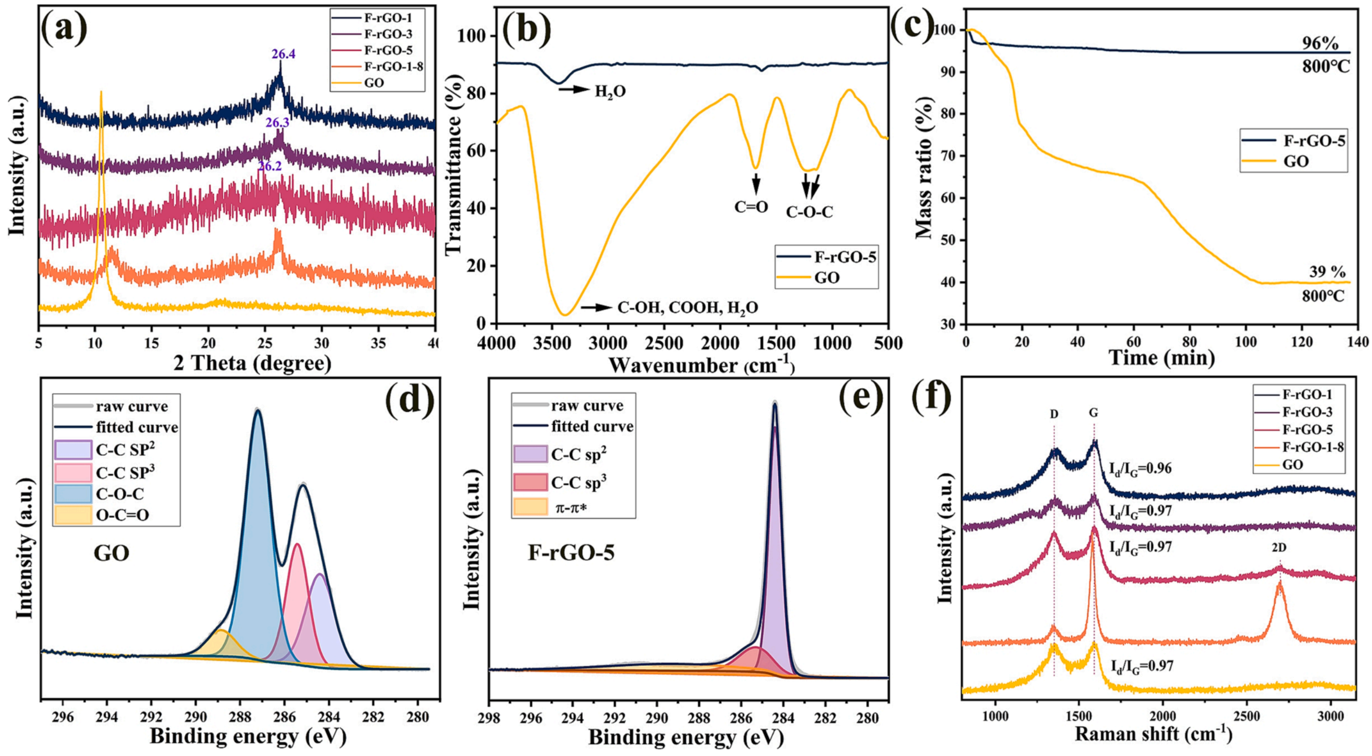

Fig. 2. **(a)** XRD patterns of F-rGO and GO. (b) FTIR, (c) TG, (d, e) high-resolution XPS spectra for C 1 s of F-rGO-5 and GO. (f) Raman spectra of F-rGO and GO.

photoelectron spectroscopy (XPS) spectrums (Fig. 2d, e, and S8) and thermogravimetric (TG) curves (Fig. 2c). The TGA curve clearly illustrates that GO was effectively reduced, with the oxygen content in the initial graphene oxide being only not more than 40 %, and the carbon content reaching 96% as the FJH proceeded. The C 1 s peaks are deconvoluted into several sub-peaks. After the FJH process, the content of sp^3 C (285.4 eV) decreases but still exists. Given that the above test results indicate that the F-rGO-5 is almost entirely C-element, only a small portion of the oxygen-containing functional groups are not completely reduced. It may represent edges and the inter-layer bridge bonds between graphene lamellae. Additionally, the appearance of π-π* satellite peak at 290 eV confirms the conjugated π-electron system in F-rGO-5. As shown in **Figure S9**, we performed XPS tests on the other three groups of samples and found that the proportion of C-C sp^2 bonds was only 55 %, 59.6 %, and 50 % (F-rGO-1, F-rGO-3 and F-rGO-1−8), respectively. The percentage of sp^2 bonds in F-rGO-5 is 66.3 %, which is the highest [28]. Raman spectroscopy (Fig. 2f) is performed to characterize defects and stacking in GO and F-rGO [29,30]. The D peak locates at 1350 cm^{-1} and is evoked by defects, while the G peak at 1580 cm^{-1} reveals the stretching vibration mode of the in-plane SP^2 carbon. In the one-time FJH reaction products, the D peak is always present, and the value of I_d/I_g is almost constant. Given that F-rGO is composed of carbon elements, the D peak indicates the defects and edge scattering in the lattice. The appearance of the 2D peak in the Raman spectrum of F-rGO-5 represents the few-layer structure, and the bump-like region (2400–2500 $cm-^1$) also demonstrates the disorder stacking of the graphene network [31].

When serving as anode materials for the Li-ion half cells, F-rGO-5 anodes display discharge capacities of 3307, 1377, 1275, and 1224 mAh/g at 1 A/g in the initial four galvanostatic charge–discharge (GCD) cycles. A large irreversible capacity in the first cycle indicates that the solid electrolyte interface (SEI) mainly forms during the first lithiation process (Fig. 3a) [12,32]. Correspondingly, two reduction peaks at 1.7 V and 0.7 V in the first cycle of the CV curve (**Figure S10a**) are attributed to the decomposition of the electrolyte on the F-rGO-5 surface. The peak at 0.7 V represents SEI generation and the peak at 1.7 V partially-reversible side reactions occur between Li^+ and some remaining surface functional groups of F-rGO [33]. The peak current (i) and scanning rate (v) in CV curves at scan rates of 0.2 to 5 mV s^{-1} are consistent with the formula:$i = av^b$, in which a and b are fitting parameters calculated from the slope of the log (i)–log (ν)curve. When b approaches 1, capacitance behavior dominates the electrochemical process; when b comes to 0.5, semi-linear diffusion takes over. The b value of C1, C2, and A1 is 0.57, 0.72, and 0.84, respectively (Fig. 3b, c), indicating the Li^+ storage is controlled jointly by capacitance and battery behaviors [34,35]. The capacitive behavior accounts for 64 % at 5 mV s^{-1} for F-rGO-5 (**Figure S10b**, the area beyond the original curve is due to the residual current and ohmic polarization [36]). To exclude the effect of

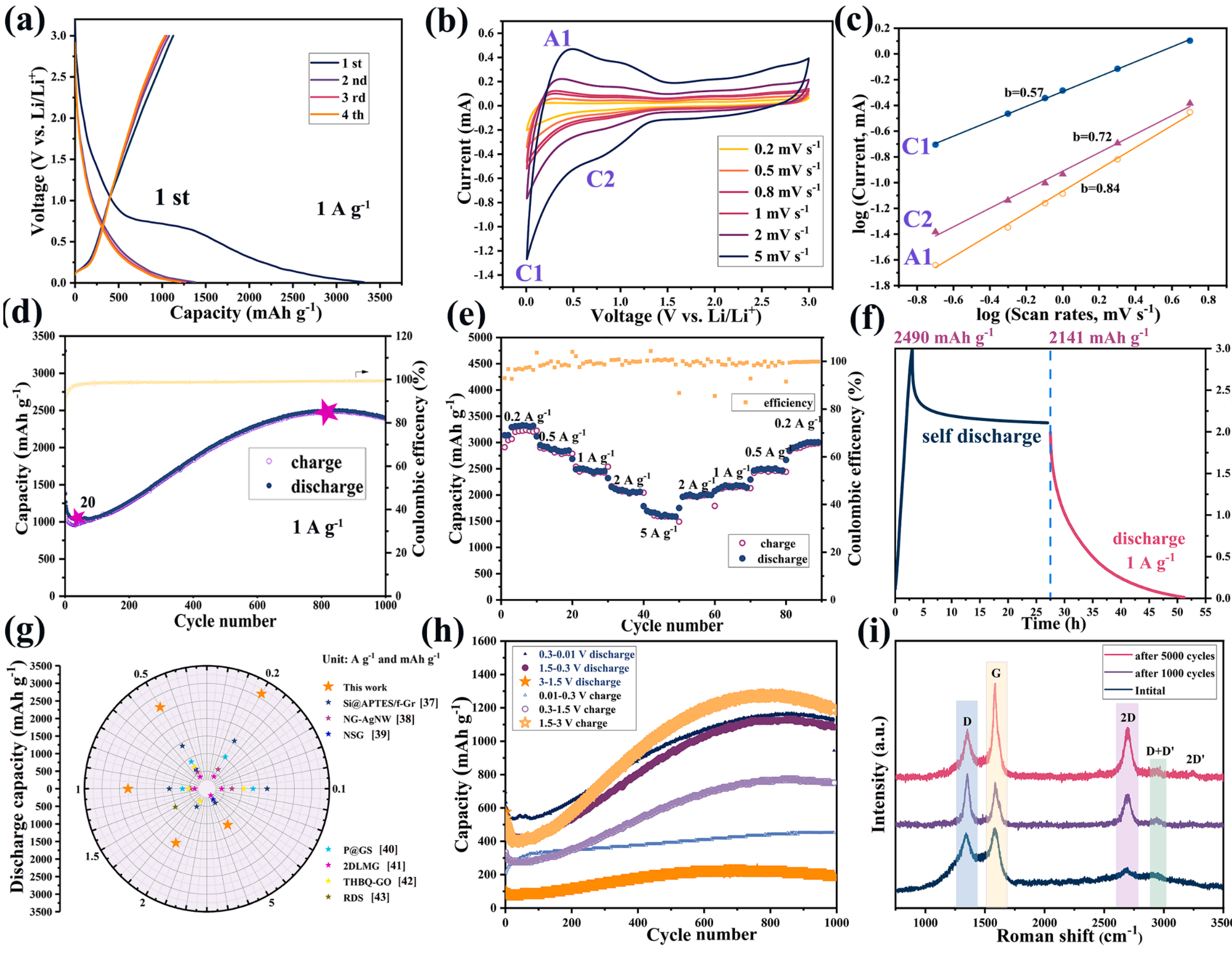

Fig. 3. (a) Charge-discharge profiles of F-rGO-5 at 1 A g-1. (b) CV curves, and (c) b value of F-rGO-5 at different scan rates. (d) Cycling performance of F-rGO-5 at 1 A g-1. (e) Rate performance and (f) self-discharge curve of 1000 GCD-cycled F-rGO-5. (g) The comparison with references. (h) Segmented capacity change during 1000 GCD cycles. (i) Raman spectra of F-rGO-5 anode after 1000 GCD (1 A g-1) and 5000 GCD (5 A g-1) cycles.

lithium-ion consumption by the SEI formed in initial cycles, a cycle test was conducted at 1 A/g (Fig. 3d). After twenty GCD cycles, the discharge capacity shift from falling to increasing with the Coulombic efficiency of ~ 100 %. The initial state battery and the battery after 1000 GCDs cycles was tested for rate performance, the initial state battery has the discharge capacities of 2556, 2059, 1480, 851, 485 mAh/g current densities of 0.2, 0.5, 1, 2, and 5 A/g, respectively. And the battery after 1000 GCDs cycles showing high discharge capacities of 3321, 2833, 2450, 2075, and 1950 mAh/g at current densities of 0.2, 0.5, 1, 2, and 5 A/g, respectively, showing an outstanding performance to previous reports (Fig. 3e, **g**, **Figure S11**) [37-43]. The self-discharge behavior was evaluated by testing the discharge curve of a fully charged battery. The voltage of the battery drop to 2.2 V after 10 h of standing and remain stable for the following 17 h (Fig. 3f). The voltage drop is attributed to the weakly adsorbed ions returning to the electrolyte driven by the electrostatic effect. A discharge capacity of 2141 mAh/g could still be released at a current density of 1 A/g after 27 h of standing, demonstrating its potential in high-capacity and stable energy storage. As a comparison, reduced graphene oxide (rGO) prepared by heating GO in an Ar-protected tube furnace at 800 °C was also tested as a lithium storage electrode under the same conditions. The capacity of rGO is only 350 mAh/g at a current density of 1 A/g, and a similar increase in capacity is not observed (**Figure S12**).

To further understand the high and increasing capacity of F-GO during cycling, the rate of charge change at constant potential change, i.e., differential capacitance (dQ/dV) is analyzed. According to the dQ/dV curve (**Figure S10c**) of the discharge process, the charge accumulation linearly relates to the voltage in the 3 V–1.5 V segment, representing the capacitive adsorption of lithium ions on the surface [44]. The capacity accumulation exhibits a mixed control of capacitive, semi-infinite diffusion at discharge voltages below 1.5 V. Considering the lithium insertion process between 0.3 V and 0.01 V, the voltage interval is divided into three segments, and 1.5 V and 0.3 V are chosen as the boundary. Define the proportion of the voltage interval's capacity to the overall capacity as the capacity ratio. We found an increasing trend in all segments, but the degree of the increment varies (Fig. 3h and S13). The capacity ratio of 3–1.5 V hardly changes throughout the cycling cycle, indicating that the structure of the electrode undergoes uniform expansion without drastic changes. Since the capacity obtained by lithium ions through the formation of lithium-carbon compounds with SP^2 C does not increase with cycling, and the above characterizations demonstrate that F-rGO contains multiple defects, then the rise in

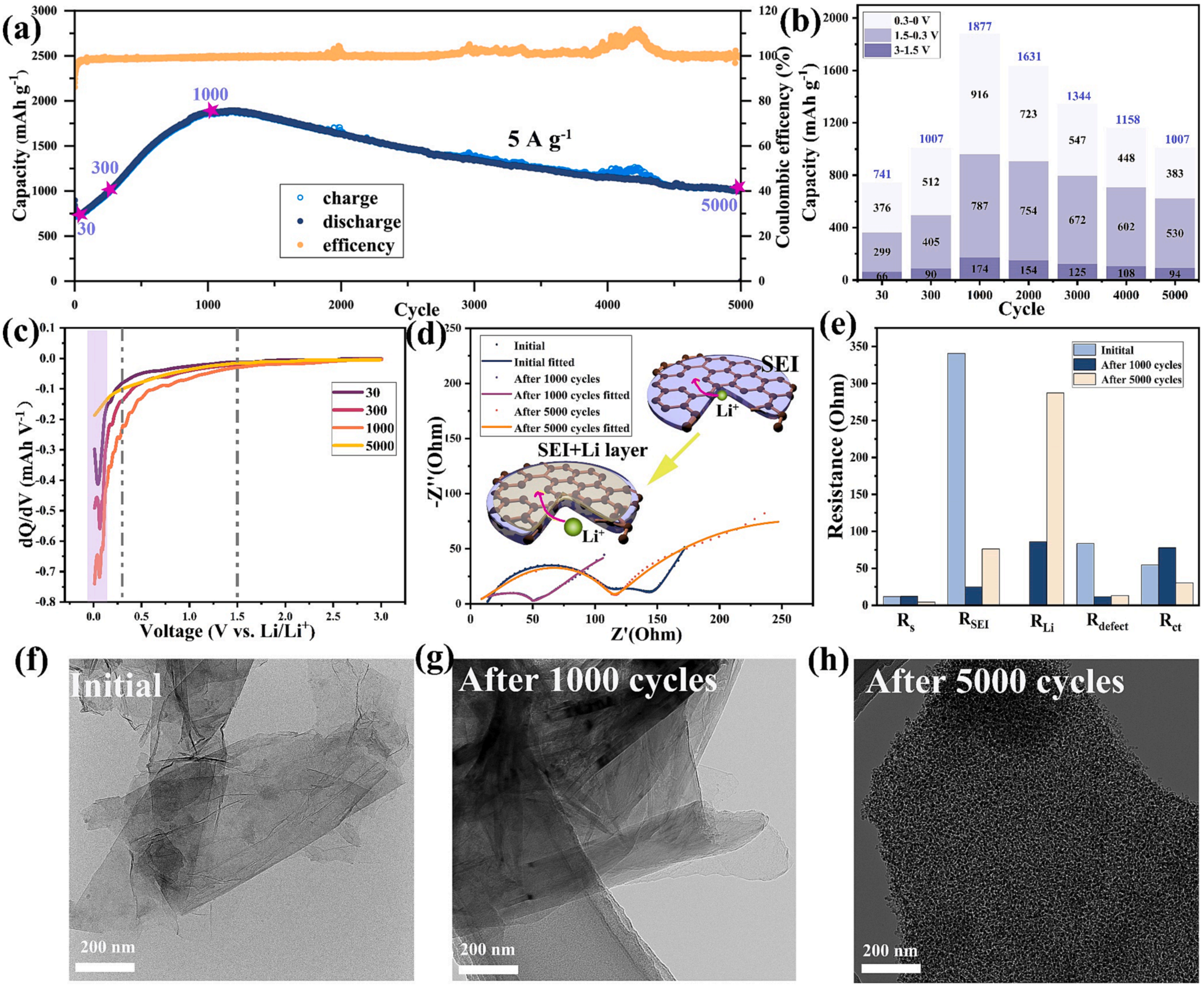

Fig. 4. (a) Long cycling performance of F-rGO-5 at 5 A/g for 5000 cycles. (d) Segmented capacity values for different cycle periods. (c)The dQ/dV curves of the 30th, 300th, 1000th, and 5000th cycle. (d) Nyquist plots of F-rGO-5 obtained from EIS spectra, insert schematic illustration of Li + transport. (e) Fitting results of EIS. TEM images of (f) initial, (g) 1000 cycled, (h) 5000 cycled F-rGO-5 at 5 A/g.

capacity of other segments may be attributed to the contribution of defects in the structure. The significant increase in the intensity of the D peak in the Raman spectrum of F-rGO-5 after 1000 GCD cycles suggests the new defects generation during cycling (Fig. 3i). According to previous reports, the maximum theoretical capacity of monolayer graphene with a 100 % Stone-Wales (SW) defect is 1100 mAh/g, and with the highest double vacancy (DV) defect of 25 %, the maximum capacity is as high as 1675 mAh/g [45]. However, the highest capacity of F-RGO-5 reaches 2500 mAh/g in the 800th cycle, indicating the existence of an additional lithium storage mechanism in F-RGO-5 electrode.

To comprehensively elucidate the energy storage mechanism of F-RGO-5, a longer cycle test was conducted at 5 A/g (Fig. 4a). The capacity first climbs and then decreases in 5000 cycles, peaking at the 1000th cycle and then steadily declining. Remarkably, new peaks are observed in the differential capacitance (dQ/dV) curves of the 300th and 100th (Fig. 4**c** and S14), which may be attributed to the reduction of lithium. Furthermore, as the defects content increase, the lithium deposition potential shows a positive shift (0.03 V at 300th and 0.04 V at 1000th). Thus, the rising in capacity during cycling is not only attributed to the increase in defects but also to the deposition of lithium layers. The stable Coulomb efficiency suggests that the deposited layer is highly reversible. At the 5000th cycle, the discharge capacity drops to 1007 mAh/g, equal to the capacity in the 300th. Despite having similar overall capacity, the capacity ratio in the 0.3–0.01 V decreased from 50 % to 39 % (Fig. 4b). Electrochemical impedance spectroscopy (EIS) is fitted by equivalent circuits (**Figure S15a** for initial data, **Figure S15b** for cycled data). R_{SEI} decreases significantly during the capacity rising stage, indicating that the formation of SEI facilitates ion conduction (Fig. 4 **d, e, and Table S2**). The appearance of R_{Li} confirms the formation of the Li deposition, as shown in Fig. 4e, and the significant increase of R_{Li} after 5000 cycles represents the formation of an irreversible lithium deposition layer. Fluctuations in Coulomb efficiency indicate that this dead lithium is shed during cycling (Fig. 4a), so the formation of lithium dendrites and their shedding are the main factors in capacity degradation. The deposited lithium layer also leads to a weakening of the intensity of the D-peak in the Raman pattern (Fig. 3i). Compared to the initial state, a layer of SEI film attach to the surface of the lamellae after 1000 cycles. In the ex-situ XPS spectra, as shown in **Figure S15a**, the peaks representing Li_2CO_3, O–C=O and C-F bonds at 290, 288.6, and 286 eV, respectively. The peaks of Li–F and P–F appearing at 684.9 and 687.4 eV in **Figure S15b**. In the high-resolution spectra of Li 1 s, the peaks at 54.8 and 55.5 eV prove the bonds of Li–F and Li_2CO_3 appeared (**Figure S15c**). The appearance of these new signals after cell cycling represents the generation of SEI. The XPS results show that the electrode has a Li content of 28 %. Since the electrodes were disassembled after charge and discharge cycles and the final step was a delithiation step, this high Li content is consistent with our hypothesized model. After 5000 cycles, a large number of holes are evenly distributed throughout the lamellae, which should be caused by deposition of large amounts of lithium ions at the defect site. The distribution phenomenon is similar to the location of the holes exhibited in the initial TEM by F-rGO-5 (Fig. 4**f-h, Figure S17**). In order to further demonstrate the potential application value of F-rGO-5, we assembled F-rGO-5 as the anode and lithium iron phosphate ($LiFePO_4$) as the cathode to form a full cell battery. In the CV images of the first four cycles (**Figure S18**), it can be found that the reduction and oxidation peaks appear at 3.55 V and 3.35 V, respectively, which correspond to the embedding and detachment potentials of lithium ions during battery charging and discharging. The full cell achieved a specific capacity of 131 mAh/g in the first discharge, retaining 82 mAh/g atter 90 GCD cycles.

As an illustration, theoretical calculations were performed using Density Functional Theory (DFT) methodology, employing classic Stone-Wales (SW) defect and single vacancy models (DV1 and DV2). In exploring the adsorption system's stability, the adsorption energy of diverse Li atoms on graphene is computed using the subsequent formula:

$$\Delta E_{ad}(Li) = E_{Li-defect} - E_{Li-defect} - E_{defect} \quad (1)$$

here, $E_{Li\text{-}defect}$, E_{defect}, and E_{Li} denote the total energies of graphene containing Li clusters, defect graphene, and individual Li atoms, respectively. As depicted in Fig. 5a, defective carbon layers exhibit lower adsorption energies compared to defect-free carbon layers, indicating the propensity for lithium to preferentially occupy these defect sites. Particularly, the adsorption energy is minimal between lithium atoms and SV1. Differential charge maps (Fig. 5b) reveal an increased electron-donating ability of carbon atoms near defects, facilitating lithium ions' easier access to electrons from carbon atoms at defect sites, elucidating the reason for lithium ion deposition above 0 V.

The intricate reaction mechanism underlying the behavior of F-rGO-5 is illustrated in Fig. 5c. The swift heating triggers the elimination of oxygen-functional groups, while the rapid annealing ensures that the high defect density is preserved. The Joule heat temperature, which is elevated, augments the reactivity of carbon atoms with dangling bonds. This, in turn, facilitates the formation of copious interlayer bridging bonds, which greatly enhance electrical conductivity. Additionally, the overlapping graphene fuse together at high temperatures, creating topological defects that are subsequently reconstructed as a tightly connected 3D network of carbon atoms. Due to the lower adsorption energy of lithium ions at these defects compared to those on intact six-membered ring carbon atoms, F-rGO exhibits a capacity that surpasses the theoretical specific capacity of graphene. Furthermore, the 3D structure of F-rGO-5 offers abundant sites for lithium ion adsorption. During the cycling process, the defects in the network increase, reducing the nucleation potential of lithium ions and promoting their deposition at the graphene defects, which forms a localized "lithium anode" [40]. The appearance of defect adsorption, reversible lithium plating, and 3D structure synergistically confer high capacity and excellent rate performance of F-rGO-5. Moreover, the strong attraction of lithium ions at the defects alleviates the self-discharge of the half-cell. After 1000 cycles at a high current of 5 A/g, defect generation saturates, and the consequent increase in local overpotential leads to the generation of dead lithium, which results in the coverage of the carbon layer and a decline in capacity. However, the closed network, linked by carbon bonds, enables the F-rGO-5 to withstand the volume expansion caused by dendrite growth. As a result, although the capacity decays, the rate of decay is not rapid, and F-rGO-5 can maintain a high capacity of 1007 mAh/g even after 5000 cycles.

3. Conclusion

In conclusion, the FJH method effectively reduces GO and drastically reduces the oxygen content, forming a 3D carbon network containing a large number of intrinsic defects. The nascent defects during cycling promote the rise in capacity, reaching as high as 2450 mAh/g (1 A/g) after 1000 cycles, with capacity at different rates higher than that of graphene modified by other methods. While the formation of dead lithium reduces capacity, the tightly connected 3D network can withstand volume expansion during negative electrode cycling, resulting in a reversible capacity of 1007 mAh/g after 5000 cycles at the current density of 5A/g. Although graphene-based lithium still faces challenges like low first efficiency and self-discharge, t this preparation method provides a new approach to designing defect engineering-based electrodes and fresh insights to comprehend changes during the cycling of comparable thin-layer electrodes.

CRediT authorship contribution statement

Shu Dong: Conceptualization, Data curation, Formal analysis, Investigation. **Yali Song:** Writing – original draft, Writing – review & editing. **Mingyu Su:** Software. **Guiling Wang:** Supervision. **Yingyi Gao:** Resources, Supervision. **Kai Zhu:** Supervision. **Dianxue Cao:**

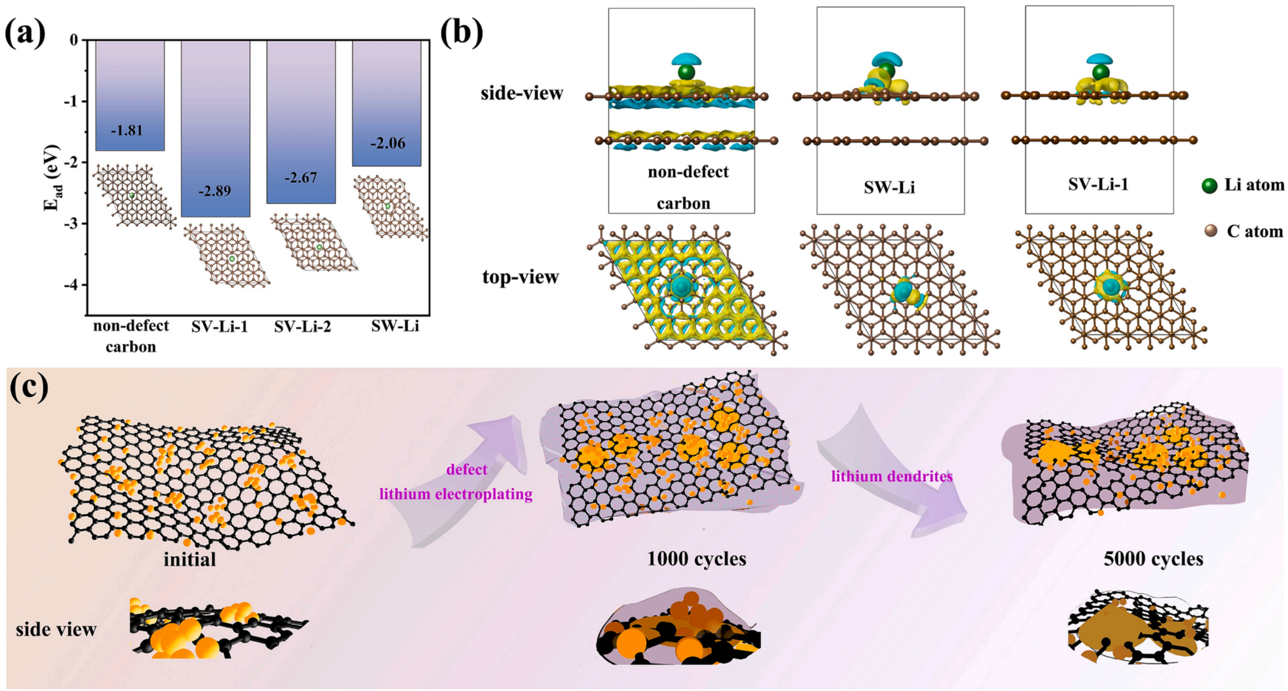

Fig. 5. (b) the corresponding differential charge density of Li adsorption site of none-defect carbon layers, SW defect, and DV defect, respectively. Yellow and cyan surfaces delineate areas signaling the gain and loss of charge, respectively (isosurface level = 0.003). The representation of lithium and carbon atoms is visually distinguished by their portrayal in green and brown hues, respectively. (c) Schematic illustration for the mechanism of F-rGO-5 anode. (For interpretation of the references to colour in this figure legend, the reader is referred to the web version of this article.)

Supervision.

Declaration of competing interest

The authors declare that they have no known competing financial interests or personal relationships that could have appeared to influence the work reported in this paper.

Data availability

Data will be made available on request.

Acknowledgements

This work was supported by the Student Research and Innovation Fund of the Fundamental Research Funds for the Central Universities, China [3072022JIP1003].

Appendix A. Supplementary data

Supplementary data to this article can be found online at https://doi.org/10.1016/j.cej.2023.147988.

References

[1] B.S.Y. Kim, A.J. Sternbach, M.S. Choi, Z. Sun, F.L. Ruta, Y. Shao, A.S. McLeod, L. Xiong, Y. Dong, T.S. Chung, A. Rajendran, S. Liu, A. Nipane, S.H. Chae, A. Zangiabadi, X. Xu, A.J. Millis, P.J. Schuck, R. Cory, J.C. Dean, D.N.B. Hone, Ambipolar charge-transfer graphene plasmonic cavities, Nat. Mater. 22 (2023) 838–843, https://doi.org/10.1038/s41563-023-01520-5.

[2] M.F. El-Kady, Y. Shao, R.B. Kaner, Graphene for batteries, supercapacitors and beyond, Nat. Rev. Mater. 1 (2016) 16033, https://doi.org/10.1038/natrevmats.2016.33.

[3] R. Raccichini, A. Varzi, D. Wei, S. Passerini, Critical insight into the relentless progression toward graphene and graphene-containing materials for lithium-ion battery anodes, Adv. Mater. 29 (2017) 1603421, https://doi.org/10.1002/adma.201603421.

[4] F.J. Sonia, M.K. Jangid, B. Ananthoju, M. Aslam, P. Johari, A. Mukhopadhyay, Understanding the Li-storage in few layers graphene with respect to bulk graphite: experimental, analytical and computational study, J. Mater. Chem. A. 5 (2017) 8662–8679, https://doi.org/10.1039/C7TA01978E.

[5] K. Ji, J. Han, A. Hirata, T. Fujita, Y. Shen, S. Ning, P. Liu, H. Kashani, Y. Tian, Y. Ito, J. Fujita, Y. Oyama, Lithium intercalation into bilayer graphene, Nat. Commun. 10 (2019) 275, https://doi.org/10.1038/s41467-018-07942-z.

[6] N. Kim, H. Cha, S. Chae, T. Lee, Y. Lee, Y. Kim, J. Sung, J. Cho, Carbide-mediated catalytic hydrogenolysis: defects in graphene on a carbonaceous lithium host for liquid and all-solid-state lithium metal batteries, Energy Environ. Sci. 16 (2023) 2505–2517, https://doi.org/10.1039/D2EE03108F.

[7] F.J. Sonia, M. Aslam, A. Mukhopadhyay, Understanding the processing-structure-performance relationship of graphene and its variants as anode material for Li-ion batteries: A critical review, Carbon 156 (2020) 130–165, https://doi.org/10.1016/j.carbon.2019.09.026.

[8] W. Liu, Y. Xia, W. Wang, Y. Wang, J. Jin, Y. Chen, E. Paek, D. Mitlin, Pristine or highly defective? Understanding the role of graphene structure for stable lithium metal plating, Adv. Energy Mater. 9 (2019), https://doi.org/10.1002/aenm.201802918.

[9] W. Wan, H. Wang, First-principles investigation of adsorption and diffusion of ions on pristine, defective and B-doped graphene, Materials 8 (2015) 6163–6178, https://doi.org/10.3390/ma8095297.

[10] L.A. De Souza, G.M. de Castro, L.F. Marques, J.C. Belchior, A DFT investigation of lithium adsorption on graphenes as a potential anode material in lithium-ion batteries, J. Mol. Graphics Modell. 108 (2021), https://doi.org/10.1016/j.jmgm.2021.107998.

[11] A.M. Ilyin, V.V. Kudryashov, N.R. Guseinov, Computer simulation of few-layer graphene intercalated by lithium for power sources, J. Electrochem. Soc. 162 (2015) A1544–A1546, https://doi.org/10.1149/2.0701508jes.

[12] J. Shao, H. Zhou, J. Feng, M. Zhu, A. Yuan, Facile synthesis of MOF-derived hollow NiO microspheres integrated with graphene foam for improved lithium-storage properties, J. Alloys Compd. 784 (2019) 869–876, https://doi.org/10.1016/j.jallcom.2019.01.157.

[13] D.X. Luong, K.V. Bets, W.A. Algozeeb, M.G. Stanford, C. Kittrell, W. Chen, R. V. Salvatierra, M. Ren, E.A. McHugh, P.A. Advincula, Z. Wang, M. Bhatt, H. Guo, V. Mancevski, R. Shahsavari, B.I. Yakobson, J.M. Tour, Gram-scale bottom-up flash graphene synthesis, Nature. 577 (2020) 647–651, https://doi.org/10.1038/s41586-020-1938-0.

[14] X. Yang, B. Wei, Exact research on the theory of the blackbody thermal radiation, Sci. Rep. 6 (2016) 37214, https://doi.org/10.1038/srep37214.

[15] M. Seyring, A. Simon, I. Voigt, U. Ritter, M. Rettenmayr, Quantitative crystallographic analysis of individual carbon nanofibers using high resolution transmission electron microscopy and electron diffraction, Carbon. 116 (2017) 347–355, https://doi.org/10.1016/j.carbon.2017.01.107.

[16] J.C. Meyer, A.K. Geim, M.I. Katsnelson, K.S. Novoselov, D. Obergfell, S. Roth, C. Girit, A. Zettl, On the roughness of single- and bi-layer graphene membranes,

Solid State Commun. 143 (2007) 101–109, https://doi.org/10.1016/j.ssc.2007.02.047.

[17] J. Ping, M.S. Fuhrer, Layer number and stacking sequence imaging of few-layer graphene by transmission electron microscopy, Nano Lett. 12 (2012) 4635–4641, https://doi.org/10.1021/nl301932v.

[18] N. Gupta, S. Walia, U. Mogera, G.U. Kulkarni, Twist-dependent Raman and electron diffraction correlations in twisted multilayer graphene, J. Phys. Chem. Lett. 11 (2020) 2797–2803, https://doi.org/10.1021/acs.jpclett.0c00582.

[19] K. Krishnamoorthy, M. Veerapandian, K. Yun, S. Kim, The chemical and structural analysis of graphene oxide with different degrees of oxidation, Carbon. 53 (2013) 38–49, https://doi.org/10.1016/j.carbon.2012.10.013.

[20] U. Mogera, R. Dhanya, R. Pujar, C. Narayana, G.U. Kulkarni, Highly decoupled graphene multilayers: turbostraticity at its best, J. Phys. Chem. Lett. 6 (2015) 4437–4443, https://doi.org/10.1021/acs.jpclett.5b02145.

[21] S. Pandey, C. Biswas, T. Ghosh, J.J. Bae, P. Rai, G.-H. Kim, K.J. Thomas, Y.H. Lee, P. Nikolaev, S. Arepalli, Transition from direct to Fowler-Nordheim tunneling in chemically reduced graphene oxide film, Nanoscale. 6 (2014) 3410–3417, https://doi.org/10.1039/C3NR05675A.

[22] M.G. Stanford, K.V. Bets, D.X. Luong, P.A. Advincula, W. Chen, J.T. Li, Z. Wang, E. A. McHugh, W.A. Algozeeb, B.I. Yakobson, J.M. Tour, Flash graphene morphologies, ACS Nano. 14 (2020) 13691–13699, https://doi.org/10.1021/acsnano.0c05900.

[23] S. Hettler, D. Sebastian, M. Pelaez-Fernandez, A.M. Benito, W.K. Maser, R. Arenal, In-situ reduction by Joule heating and measurement of electrical conductivity of graphene oxide in a transmission electron microscope, 2D Mater. 8 (2021), 031001, https://doi.org/10.1088/2053-1583/abedc9.

[24] J.Y. Huang, F. Ding, B.I. Yakobson, P. Lu, L. Qi, J. Li, In situ observation of graphene sublimation and multi-layer edge reconstructions, Proc. Natl. Acad. Sci. 106 (2009) 10103–10108, https://doi.org/10.1073/pnas.0905193106.

[25] P. Wang, H. Zhou, C. Meng, Z. Wang, K. Akhtar, A. Yuan, Cyanometallic framework-derived hierarchical Co3O4-NiO/graphene foam as high-performance binder-free electrodes for supercapacitors, Chem. Eng. J. 369 (2019) 57–63, https://doi.org/10.1016/j.cej.2019.03.080.

[26] E. Sheka, N. Popova, Virtual vibrational analytics of reduced graphene oxide, Int. J. Mol. Sci. 23 (2022), https://doi.org/10.3390/ijms23136978.

[27] R. Al-Gaashani, A. Najjar, Y. Zakaria, S. Mansour, M.A. Atieh, XPS and structural studies of high quality graphene oxide and reduced graphene oxide prepared by different chemical oxidation methods, Ceram. Int. 45 (2019) 14439–14448, https://doi.org/10.1016/j.ceramint.2019.04.165.

[28] T.R. Gengenbach, G.H. Major, M.R. Linford, C.D. Easton, Practical guides for x-ray photoelectron spectroscopy (XPS): Interpreting the carbon 1s spectrum, J. Vac. Sci. Technol. 39 (2021), 013204, https://doi.org/10.1116/6.0000682.

[29] C. Gómez-Navarro, R.T. Weitz, A.M. Bittner, M. Scolari, A. Mews, M. Burghard, K. Kern, Electronic transport properties of individual chemically reduced graphene oxide sheets, Nano Lett. 7 (2007) 3499–3503, https://doi.org/10.1021/nl072090c.

[30] R. Beams, L.G. Cançado, L. Novotny, Raman characterization of defects and dopants in graphene, J. Phys.: Condens. Matter. 27 (2015), 083002, https://doi.org/10.1088/0953-8984/27/8/083002.

[31] P. Huang, R. Zhu, X. Zhang, W. Zhang, Effect of free radicals and electric field on preparation of coal pitch-derived graphene using flash Joule heating, Chem. Eng. J. 450 (2022), 137999, https://doi.org/10.1016/j.cej.2022.137999.

[32] J. Shao, J. Feng, H. Zhou, A. Yuan, Graphene aerogel encapsulated Fe-Co oxide nanocubes derived from Prussian blue analogue as integrated anode with enhanced Li-ion storage properties, Appl. Surf. Sci. 471 (2019) 745–752, https://doi.org/10.1016/j.apsusc.2018.12.040.

[33] Y. Zhou, M. Su, X. Yu, Y. Zhang, J.-G. Wang, X. Ren, R. Cao, W. Xu, D.R. Baer, Y. Du, O. Borodin, Y. Wang, X.-L. Wang, K. Xu, Z. Xu, C. Wang, Z. Zhu, Real-time mass spectrometric characterization of the solid–electrolyte interphase of a lithium-ion battery, Nat. Nanotechnol. 15 (2020) 224–230, https://doi.org/10.1038/s41565-019-0618-4.

[34] M.J. Lee, K. Lee, J. Lim, M. Li, S. Noda, S.J. Kwon, B. DeMattia, B. Lee, S.W. Lee, Outstanding low-temperature performance of structure-controlled graphene anode based on surface-controlled charge storage mechanism, Adv. Funct. Mater. 31 (2021) 2009397, https://doi.org/10.1002/adfm.202009397.

[35] S. Dong, Y. Song, Y. Fang, K. Zhu, K. Ye, Y. Gao, J. Yan, G. Wang, D. Cao, Microwave-assisted synthesis of carbon dots modified graphene for full carbon-based potassium ion capacitors, Carbon. 178 (2021) 1–9, https://doi.org/10.1016/j.carbon.2021.02.094.

[36] X. Pu, D. Zhao, C. Fu, Z. Chen, S. Cao, C. Wang, Y. Cao, understanding and calibration of charge storage mechanism in cyclic voltammetry curves, Angew. Chem., Int. Ed. 60 (2021) 21310–21318, https://doi.org/10.1002/anie.202104167.

[37] Y. Zhang, Y. Cheng, J. Song, Y. Zhang, Q. Shi, J. Wang, F. Tian, S. Yuan, Z. Su, C. Zhou, Y. Wang, S. Yang, Functionalization-assistant ball milling towards Si/graphene anodes in high performance Li-ion batteries, Carbon. 181 (2021) 300–309, https://doi.org/10.1016/j.carbon.2021.05.024.

[38] D. Cai, C. Wang, C. Shi, N. Tan, Facile synthesis of N and S co-doped graphene sheets as anode materials for high-performance lithium-ion batteries, J. Alloys Compd. 731 (2018) 235–242, https://doi.org/10.1016/j.jallcom.2017.10.043.

[39] A.K. Nair, I. Elizabeth, G.S.S. Thomas, N. Kalarikkal, Nitrogen doped graphene – Silver nanowire hybrids: An excellent anode material for lithium ion batteries, Appl. Surf. Sci. 428 (2018) 1119–1129, https://doi.org/10.1016/j.apsusc.2017.09.214.

[40] S. Ding, W. Cheng, L. Zhang, G. Du, X. Hao, G. Nie, B. Xu, M. Zhang, Q. Su, C. A. Serra, Organic molecule confinement reaction for preparation of the Sn nanoparticles@graphene anode materials in Lithium-ion battery, J. Colloid Interface Sci. 589 (2021) 308–317, https://doi.org/10.1016/j.jcis.2020.12.086.

[41] L. Wang, H. Guo, W. Wang, K. Teng, Z. Xu, C. Chen, C. Li, C. Yang, C. Hu, Preparation of sandwich-like phosphorus/reduced graphene oxide composites as anode materials for lithium-ion batteries, Electrochim. Acta. 211 (2016) 499–506, https://doi.org/10.1016/j.electacta.2016.06.052.

[42] Y. Wang, X. Li, L. Chen, Z. Xiong, J. Feng, L. Zhao, Z. Wang, Y. Zhao, Ultrahigh-capacity tetrahydroxybenzoquinone grafted graphene material as a novel anode for lithium-ion batteries, Carbon 155 (2019) 445–452, https://doi.org/10.1016/j.carbon.2019.09.011.

[43] D.W. Kim, S.M. Jung, C. Senthil, S.-S. Kim, B.-K. Ju, H.Y. Jung, Understanding excess Li storage beyond LiC 6 in reduced dimensional scale graphene, ACS Nano. 15 (2021) 797–808, https://doi.org/10.1021/acsnano.0c07173.

[44] F.J. Sonia, H. Kalita, M. Aslam, A. Mukhopadhyay, Correlations between preparation methods, structural features and electrochemical Li-storage behavior of reduced graphene oxide, Nanoscale. 9 (2017) 11303–11317, https://doi.org/10.1039/C7NR03348F.

[45] D. Datta, J. Li, N. Koratkar, V.B. Shenoy, Enhanced lithiation in defective graphene, Carbon. 80 (2014) 305–310, https://doi.org/10.1016/j.carbon.2014.08.068.